Instabilities and Nonlinear *L–I* Characteristics in Complex-Coupled DFB Lasers with Antiphase Gain and Index Gratings

Björn Jonsson, Arthur James Lowery, *Senior Member, IEEE,* Henning Olesen, and Bjarne Tromborg, *Member, IEEE*

Abstract— **Complex-coupled DFB lasers can be designed to provide large bandwidths and low chirp by adjusting the strength and phase of their index and gain gratings. In this paper we develop a self-consistent method of calculating the coupling coefficient of complex-coupled DFB lasers with a corrugated active region. Basic geometrical and structural parameters are used as inputs to the model. We show that antiphase coupling implies lasing on the short-wavelength side of the Bragg wavelength which in turn leads to instabilities and/or nonlinearities in the light-current characteristic. The critical output power for onset of instabilities is typically in the order of a few milliwatts. Time-domain simulations are used to assess the potential effects of these instabilities on optical communication systems. We find that transitions from a state of equal output powers from the facets to a state of dramatically different output powers occur within a few nanoseconds of turn-on. The origin of these instabilities is explained using a simple physical model and possible ways of increasing the critical power for instabilities are discussed. For example, we clearly show that the critical power for instability increases when the carrier lifetime is decreased.**

I. Introduction

Distributed feedback (DFB) semiconductor lasers have a built-in periodic longitudinal variation of the refractive index and/or the net optical gain. This modulation produces a coupling between the forward- and backward-traveling optical waves, providing the feedback mechanism for lasing with a wavelength determined by the period of the modulation. It is well-known that index-coupled DFB lasers with antireflection coated facets have two degenerate modes, unless the waveguide contains a perturbation, such as a phase-shift or a taper. As was shown by Kogelnik and Shank [1], DFB lasers with pure gain coupling prefer a single mode of oscillation. A very high side mode suppression ratio (SMSR) can be achieved in gain-coupled or complex-coupled DFB lasers, and this is one of the main reasons for the current interest in these devices [2]–[14]. Furthermore, numerical studies of complex-coupled lasers have shown that by adjusting the ratio and phase of the gain and index gratings to give "antiphase" coupling, chirp can be reduced [4], [6] and the modulation bandwidth can be improved [15], [16].

Schatz [17] found that *conventional* index-coupled DFB lasers lasing at the short-wavelength side of the Bragg wavelength have the potential of becoming unstable when biased above some critical output power. He also showed that these instabilities cannot occur when the laser is operated on the long-wavelength side and that the instabilities become increasingly pronounced as the lasing mode is pushed away from the Bragg wavelength toward the short-wavelength side, for example by changing the magnitude of a discrete phase shift. A simple threshold analysis was given in [17] to estimate the critical output power above which instabilities occur. Instabilities in conventional index-coupled DFB lasers were also studied extensively by Olesen *et al.* [18]–[20]. We have previously found [21] that complex-coupled DFB lasers with antiphase coupling show a qualitatively similar type of instability to that reported in [17]. Lowery and Novak [11] as well as Zhang and Carroll [16] have recently performed above-threshold calculations of the dynamic properties of complex-coupled lasers, but unstable behavior was not addressed.

In this paper, a detailed analysis of DFB lasers with a complex coupling coefficient is presented. Above-threshold stability is studied using two different computer simulation programs: a semianalytic model based on the traveling-wave approach [22], and a large-signal analysis with the transmission-line laser model (TLLM) [11]. Previously, these models have been used to simulate index-coupled [19], [20], [23] and complex-coupled lasers [6], [11], [15], [21], [24], and the combined features of the two models yield detailed information about the laser's behavior.

We show that complex-coupled DFB lasers optimized for high bandwidth and low chirp, using antiphase coupling, will oscillate on the short wavelength side of the Bragg wavelength. Due to this fact, such lasers will be susceptible to instabilities and nonlinear behavior [19], [21]. This is unfortunate as we shall show that for some grating geometries the laser may become unstable at a critical output power of only a few milliwatts. The dynamics of such unstable lasers are simulated and the output powers at the two facets are found to deviate from each other after a few nanoseconds. In order to identify laser designs less susceptible to instabilities, we extend our analysis to lasers with various corrugation geometries of the active region, and show that the critical output power can be increased by altering the modulation depth and duty cycle of

Manuscript received July 18, 1995; revised January 23, 1996. This work was supported by the Australian Department of Industry, Science and Technology, under an International Science & Technology Grant.

B. Jonsson, H. Olesen, and B. Tromborg are with Tele Danmark Research, DK-2970 Hørsholm, Denmark.

A. J. Lowery is with the Photonics Research Laboratory, Australian Photonics Cooperative Research Centre, Department of Electrical and Electronic Engineering, University of Melbourne, Parkville, Vic. 3052, Australia.

Publisher Item Identifier S 0018-9197(96)03207-1.

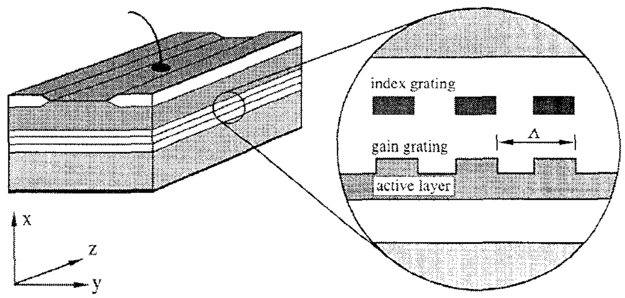

Fig. 1. Grating structure in a complex-coupled DFB laser.

the gain grating. We also develop a simple physical model of the instability mechanism, and use this model to identify methods of increasing the critical output power. Spontaneous recombination is an important damping mechanism and we find that the critical power is inversely proportional to the carrier lifetime.

The paper is organized as follows. In Section II the theoretical background for the self-consistent calculation of the complex coupling coefficient as a function of the grating geometry is presented. Section III gives a brief description of the two numerical methods. In Section IV, results for the dependence of the complex coupling coefficient on the grating geometry, below and at threshold, are presented. In Section V, operation above threshold is investigated. In particular, unstable regions are analyzed and the time-domain behavior of such lasers is simulated. The origin of these instabilities and possible ways of increasing the critical output power are discussed in Section VI. Finally, our results are summarized in Section VII.

II. Theory

Complex coupling can be realized by incorporating a periodic modulation of the active region itself, or by having separate grating layers to provide loss or index coupling. A typical multilayer laser structure is outlined in Fig. 1. The longitudinal coordinate is denoted by z, and Λ is the grating period. The active region provides gain coupling with some parasitic index coupling. The index grating allows the amount of index coupling to be independently controlled. In the following, we only use the longitudinal dependence z explicitly to denote variations *within one grating period.* It is implicitly assumed that all variables are allowed to vary slowly with z (over several grating periods).

A. Arbitrary Grating Geometry

The complex wavenumber, k, for the fundamental transverse mode is taken as

$$k(z) = \beta(z) + \frac{j}{2}\,[g(z) - \alpha_i(z)] \tag{1}$$

where g and α_i are the *local* values of the *modal* gain and internal absorption. The (real) propagation constant is expressed as

$$\beta(z) = \frac{2\pi n_{\text{eff}}(z)}{\lambda} \tag{2}$$

where n_{eff} is the waveguide effective index, and λ is the lasing wavelength. The periodic structure of Fig. 1 can be represented by periodic perturbations of the waveguide effective index, the modal gain and the internal absorption. The standard technique is to expand this perturbation in a Fourier series and to retain only the first-order terms

$$n_{\text{eff}}(z) = n_{\text{eff},0} + A_n\,\Delta n_{\text{eff}}\,\cos\left(2\pi\frac{z}{\Lambda} + \varphi_g\right) \tag{3a}$$

$$g(z) = g_0 + A_g\,\Delta g\,\cos\left(2\pi\frac{z}{\Lambda} + \varphi_g\right) \tag{3b}$$

$$\alpha_i(z) = \alpha_{i0} + A_L\,\Delta\alpha_i\,\cos\left(2\pi\frac{z}{\Lambda} + \varphi_g\right) \tag{3c}$$

where $n_{\text{eff},0}$, g_0, and α_{i0} denote the average values over one grating period; Δn_{eff}, Δg, and $\Delta\alpha_i$ are the peak-to-peak deviations within one grating period; φ_g is a phase offset of the corrugation relative to the left end-facet ($z = 0$). The detailed geometry is represented by the Fourier coefficients A_n, A_g, and A_L for the index-, gain-, and loss-gratings, respectively. Note that using the explicit forms (3a)–(3c) implies that the three types of gratings cannot have an arbitrary phase relationship. They must either be in-phase or in antiphase with each other, which will be the case for all practical geometries. It is important to realize that a variation of, for example, the active region parameters affects the refractive index and the absorption as well as the gain. All three of the modal parameters (n_{eff}, g, and α_i) depend on the material parameters of all transverse layers within the intensity profile and, in addition, may depend on the injected carrier density.

Inserting (3a)–(3c) in (1) and collecting the slowly-varying and first-order terms, the perturbation of the complex wavenumber is given as

$$k(z) = \tilde{k} + 2\,\kappa\,\cos\left(2\pi\frac{z}{\Lambda} + \varphi_g\right) \tag{4}$$

where $\tilde{k}$ is the slowly varying part of the wavenumber. We have here introduced the complex coupling coefficient κ, and in the presence of all three perturbations the general expression for κ is

$$\kappa = \frac{\pi}{\lambda}\,A_n\,\Delta n_{\text{eff}} + \frac{j}{4}\,(A_g\,\Delta g - A_L\,\Delta\alpha_i). \tag{5}$$

The real part of the coupling coefficient (the *index coupling*) is determined completely by the variation in the waveguide effective index, while the imaginary part (the *gain* or *loss coupling*) is determined by the gain and loss gratings.

The above formalism is generally applicable to DFB laser structures with complex coupling, but to proceed one has to distinguish between various laser geometries. There are at least three major categories of complex-coupled DFB lasers:

I) devices with a corrugated active region to provide gain coupling [25];

II) devices with a homogeneous active region and a separate grating layer to provide a carrier-dependent gain or loss coupling [3], [12], [14], [26];

III) devices with a homogeneous active region and a separate grating layer providing a carrier-independent loss coupling [13], [27].

All three types may have an optional index-compensating grating layer to adjust the index coupling coefficient.

For both Type I and Type II lasers, carrier dynamics are essential to describe the device behavior. Type I devices only require one population of carriers in the active region (neglecting quantum well effects such as carrier transport and carrier capture), that is, the carrier density is assumed to be constant in the transverse direction. Type II devices have two populations of carriers in the active region and the grating region, and rate equations describing their interaction must be set up. The carrier density dependence of gain or loss in the grating region must also be described. For Type III devices, the carrier dynamics in the active region are still important, but the coupling coefficient can be assumed to be independent of the carrier density. In this work we concentrate on Type I devices.

The waveguide effective index and the material gain vary with the carrier density in the active region, and the detailed variation within one grating period is described by the confinement factor $\Gamma_a(z)$. We assume that the waveguiding effect is governed by a separate confinement region in which the active region is embedded. This means that the transverse mode profile is assumed to be constant, regardless of the variations in index and gain within a grating period and changes in carrier density. The variation of $\Gamma_a(z)$ will therefore simply be given by the variation of the active region thickness. Hence

$$n_{\text{eff}}(z) = n_{\text{eff, ref}}(z) + \Gamma_a(z)\,\frac{dn}{dN}\,(N - N_{\text{ref}}) \tag{6a}$$

$$g(z) = \Gamma_a(z)\, g_m(N) \tag{6b}$$

$$\alpha_i(z) = \Gamma_a(z)\,\alpha_a + [1 - \Gamma_a(z)]\,\alpha_c \tag{6c}$$

where α_a and α_c are the material losses in the active and cladding layers, respectively. The material gain is taken as $g_m(N) = a\,(N - N_0)$, where N_0 is the transparency carrier density and a is the linear material gain coefficient. Furthermore, the waveguide effective index, $n_{\text{eff, ref}}$, is assumed to be known at some reference carrier density, N_{ref}, and the differential refractive index is denoted dn/dN. The values to be used for Δn_{eff}, Δg, and $\Delta\alpha_i$ in (5) are simply taken as the peak-to-peak values of the quantities in (6a)–(6c).

B. Rectangular Grating

To simplify the expressions further we shall only consider *rectangular* gratings with a duty cycle of γ, where $0 < \gamma < 1$. From the schematic close-up of one grating period in Fig. 2 we write the confinement factor in the active region as

$$\Gamma_a(z) = \begin{cases} \Gamma_{a,1} & \text{Region 1}\,(0 < z < \gamma\Lambda) \\ \Gamma_{a,2} & \text{Region 2}\,(\gamma\Lambda < z < \Lambda) \end{cases} \tag{7}$$

where $\Gamma_{a,1}$ and $\Gamma_{a,2}$ are the transverse confinement factors in each of the two regions. Furthermore, since we have a rectangular grating, we assume that the three Fourier components are equal:

$$A_g = A_n = A_L = \frac{2}{\pi}\,\sin(\pi\,\gamma). \tag{8}$$

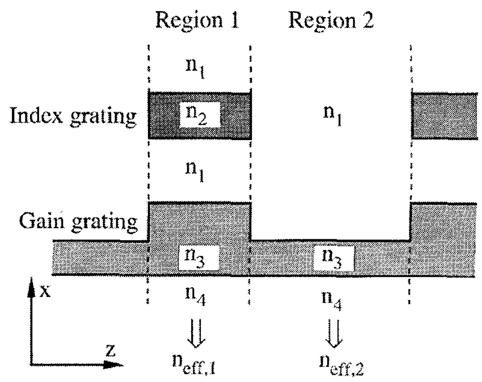

Fig. 2. Close-up of the refractive index profile for a complex-coupled DFB laser with a rectangular grating profile and index grating compensation.

Expressions for the index coupling coefficient, κ_i, and gain coupling coefficient, κ_g, can be obtained from (5):

$$\kappa_i = \frac{2}{\lambda}\,\sin(\pi\gamma) \cdot \left[\Delta n_{\text{eff, ref}} + \Delta\Gamma_a\,\frac{dn}{dN}\,(N - N_{\text{ref}})\right] \tag{9a}$$

$$\kappa_g = \frac{1}{2\pi}\,\sin(\pi\gamma)\Delta\Gamma_a(g_m + \alpha_c - \alpha_a) \tag{9b}$$

where we have denoted the waveguide effective index difference between regions 1 and 2 ("the built-in effective index step") as $\Delta n_{\text{eff, ref}}$ and have used $\Delta\Gamma_a$ for the confinement factor difference (i.e., $\Delta\Gamma_a = \Gamma_{a,1} - \Gamma_{a,2}$). The waveguide effective index can be calculated by standard methods, if the dimensions and compositions of the epitaxial layers are specified. However, for simplicity, we have assumed that $\Delta n_{\text{eff, ref}}$ is explicitly known at the reference carrier density.

Equations (9a) and (9b) give the fundamental relationship between the coupling coefficient and the structure of the grating layers. These equations are valid below and above threshold, and the sign of both coupling coefficients can be negative. Opposite signs of κ_i and κ_g imply that the phase of the index grating is shifted by π relative to the gain grating; this is an "antiphase" grating. Equal signs imply an "in-phase" grating [4].

The modulation depth of the corrugated active region is defined as

$$m = \frac{d_{a,1} - d_{a,2}}{d_{a,1} + d_{a,2}} \tag{10}$$

where $d_{a,1}$ and $d_{a,2}$ are the thicknesses of each region. A modulation depth of zero corresponds to a purely index-coupled DFB laser ($\kappa_g = 0$), while 100% modulation depth denotes a complex-coupled DFB laser with an on-off gain grating (i.e., $d_{a,2} = 0$). The average thickness of the active region is related to the duty cycle of the grating by

$$d_{\text{avg}} = \gamma\, d_{a,1} + (1 - \gamma)d_{a,2}. \tag{11}$$

Similarly, the average confinement factor for the active region is $\tilde{\Gamma} = \gamma\Gamma_{a,1} + (1 - \gamma)\Gamma_{a,2}$.

C. The Carrier Density Rate Equation

Since we are dealing with a nonuniform active region, it is essential to specify precisely how the carrier injection is treated, as this seems to have given rise to some confusion in the literature.

A key assumption in our work is that carriers cannot bypass the active region, hence the injection efficiency into the active region is always set to 100%. Furthermore, the injected carriers are assumed to be evenly distributed over the total active volume within a grating period, and an average carrier density is calculated. Spatial holeburning effects are included in the usual way by allowing the average carrier density to vary slowly along the cavity.

The laser is assumed to have a single electrode extending over the total laser chip length, L. If the active region width is denoted by w, the *average* cross-sectional area of the active region is $A_c = w\, d_{\text{avg}}$. Neglecting any noise terms, the rate equation for the carrier density becomes

$$\frac{dN}{dt} = \frac{I}{e\,A_c\,L} - R_{\text{sp}}(N) - R_{st,\,0}(N,\, u^+,\, u^-) - R_{st,\,g}(N,\, u^+,\, u^-) \tag{12}$$

where I is the bias current, e is the electron charge, R_{sp} is the spontaneous recombination rate, $R_{st,\,0}$ is the usual stimulated recombination rate, and $R_{st,\,g}$ is the extra contribution to the stimulated recombination rate due to the standing-wave effect [22], [28]. The traveling waves propagating in the positive and negative directions are denoted u^+ and u^-, respectively. Thus

$$R_{\text{sp}}(N) = AN + BN^2 + CN^3 \tag{13a}$$

$$R_{st,\,0}(N,\, u^+,\, u^-) = \frac{2\varepsilon_0 c n_{\text{eff},\,0}}{\hbar\omega A_c}\, g_m \tilde{\Gamma} \cdot (|u^+|^2 + |u^-|^2) \tag{13b}$$

$$R_{st,\,g}(N,\, u^+,\, u^-) = \frac{2\varepsilon_0 c n_{\text{eff},\,0}}{\hbar\omega A_c}\, g_m \Delta\Gamma_a \frac{\sin(\pi\gamma)}{\pi} \cdot [e^{+j\varphi_g} u^+ (u^-)^* + c.c.] \tag{13c}$$

where A, B, and C are the usual recombination coefficients, c is the light velocity in vacuum, ε_0 is the vacuum permittivity, and $\hbar\omega$ is the photon energy.

The photon density, S, and the output powers from the left and right facets, P_L and P_R, are related to u^+ and u^- by the following expressions [22]

$$S = \frac{2\varepsilon_0 n_{\text{eff},\,0} n_g}{\hbar\omega A_{\text{ph}}} (|u^+|^2 + |u^-|^2|) \tag{14a}$$

$$P_L = 2\varepsilon_0 c n_{\text{eff},\,0}(1 - R_1)|u^-(z=0)|^2 \tag{14b}$$

$$P_R = 2\,\varepsilon_0\, c n_{\text{eff},\,0}\,(1 - R_2)|u^+(z=L)|^2 \tag{14c}$$

where $A_{\text{ph}} = A_c/\tilde{\Gamma}$ is the average cross-sectional area of the transverse photon distribution, n_g is the group refractive index, and R_1 and R_2 are the reflectivities of the left and right facets, respectively.

Using the detailed expressions (9a), (9b), (13b), and (13c), steady-state and time-domain properties can be obtained by solving for the fields (u^+ and u^-) in the usual coupled wave equations [11], [22].

III. Numerical Approach

We have used two different computer models to simulate the behavior of complex-coupled DFB lasers; the traveling wave method (TWM) and the transmission-line laser model (TLLM). Both models can calculate the stationary distributions under given bias conditions, including longitudinal spatial holeburning and full details about the longitudinal variations in the laser cavity.

A. The traveling-Wave Method (TWM)

The traveling-wave method is a semianalytical technique, which can be used to simulate a large variety of advanced laser structures, including multisection and multielectrode configurations. Details of the method are given in [22], which also includes the analytic expressions that are required for treatment of gain-coupled devices. The stationary distributions of the photon and carrier densities are obtained by numerical integration of the coupled wave equations with boundary conditions, simultaneously solving the rate equation for the local carrier density at any position along the cavity. There may be many stationary solutions (modes) but there are usually only a few (if any) that can represent lasing modes. As discussed in detail in [19], a mode can be dominant/nondominant and stable/unstable. This classifies the modes into four groups, one for each combination, and the potential lasing modes belong to the group of dominant *and* stable modes. This rule only applies if the frequency spacings between the modes are substantially larger than the inverse carrier lifetime, but that will generally be fulfilled for laser cavity lengths below say 5 mm.

In order to decide whether a mode is dominant or not, we solve the coupled wave equations for complex frequencies and a fixed carrier distribution given by the mode. It is called dominant if *all* solutions (except that for the mode itself) lie in the upper half of the complex frequency plane [19]. Each of these solutions corresponds to a side mode, with side mode suppression ratio proportional to the imaginary part of the frequency [29]. The stability of a mode is determined from a small-signal analysis, where the induced perturbations of the relative amplitude and the phase of the output field from the facets are calculated by the use of Green's functions. The small-signal analysis results in a stability parameter, the sign of which indicates whether the mode is stable with respect to small-scale fluctuations [22].

The time domain characteristics can be investigated with, for example, the TLLM. A time-domain simulation of the laser equation (including noise terms) will usually show a transition to a dominant and stable mode, independently of the initial conditions [20]. If there are no modes which are both dominant and stable, the time-domain solution will be nonstationary, for example pulsating or chaotic, and the spectrum will be multimoded.

The semianalytic nature of the TWM allows a quick and easy mapping of laser behavior over a wide range of operating conditions, and stable and unstable regions of operation can easily be identified. Several additional characteristics can be obtained as output from a simulation, for example the lasing mode position relative to the Bragg wavelength, the local modulation responses [30], [31], and the grating filter functions [32].

B. The Transmission-Line Laser Model (TLLM)

The transmission-line laser model is a large-signal time-domain model [33]. The optical wave-guide is modeled by a transmission-line divided into sections, where each section represents a longitudinal slice of the device. Scattering matrices within each section model the optical properties of that section by modifying the optical traveling fields as they propagate from section to section at each iteration. After scattering, the fields are passed to adjacent sections via lossless transmission lines representing the optical propagation delays along the cavity so that they arrive for the next iteration. The output of the model is a time-series of optical field samples from which the optical spectrum may be obtained using Fourier transforms. Alternatively, the output field may be squared and averaged to find the power waveform. The model is very efficient for calculating laser dynamics over a wide spectral bandwidth because the optical field is not restricted to a specific modal expansion. For the same reason, the depletion of the carrier density by stimulated emission is also calculated for all spectral components of the field. The model includes random noise generators to represent spontaneous emission.

As shown in [11], special care has to be taken when applying the TLLM to gain-coupled lasers as the overlap of the standing wave within the cavity and the gain grating has to be calculated. The gain coupling is represented by scattering at the center of the model sections, which can be thought of as being due to a conductance across the transmission lines. The index coupling is represented by scattering at the section boundaries. The 90° phase difference between the two coupling mechanisms is in effect represented by the propagation delays of the transmission lines. To minimize computation time, only 21 sections are used to model the hundreds of grating periods of the real laser. This is acceptable, as the coupling of the laser's grating is represented by a harmonic of the model grating, and the carrier density varies slowly along the cavity.

IV. Results

To illustrate the longitudinal variations of the index- and gain coupling coefficients above threshold, we performed a calculation for a laser with the parameter values given in Table I and grating parameters according to Column A of Table II. These correspond to a typical 300 μm long DFB laser with a homogeneous grating structure. The laser has a threshold current of approximately 13 mA and the coupling strength, $|\kappa| L$, (at threshold) is 1.5.

Fig. 3 shows that the coupling coefficient is homogeneous when operated close to threshold, but as the bias current is increased the coupling coefficient becomes increasingly nonuniform along the cavity. This variation of the coupling coefficient is consistent with the calculated variation of the carrier density N, cf., (9a) and (9b). At 50 mA the carrier density varies between 2.83×10^{24} m^{-3} and 3.40×10^{24} m^{-3}, a range which can be considered as typical with the

TABLE I
PARAMETER VALUES USED IN THE CALCULATIONS (UNLESS STATED OTHERWISE)

Parameter	Symbol	Value	Unit
Grating duty cycle	γ	0.5	
Grating period	Λ	242.6	nm
Reflectivity of end facets	R_1, R_2	1.0×10^{-6}	
Initial grating phase	φ_g	0.0	rad
Laser chip length	L	300	μm
Active region width	w	3.5	μm
Differential refractive index	dn/dN	-3.454×10^{-26}	m^3
Linear material gain coefficient	a	7.0×10^{-20}	m^2
Linewidth enhancement factor	α	4.0	
Nonlinear gain coefficient	ε	3×10^{-23}	m^3
Transparency carrier density	N_0	1.5×10^{24}	m^{-3}
Reference carrier density	N_{ref}	0.0	m^{-3}
Waveguide effective index	$n_{eff,ref}$	3.2	
Waveguide group refractive index	n_g	3.75	
Linear recombination coefficient	A	0.0	s^{-1}
Bimolecular recombination coefficient	B	1.0×10^{-16}	m^{3}s^{-1}
Auger recombination coefficient	C	3.0×10^{-41}	m^{6}s^{-1}
Population inversion parameter	n_{sp}	2.0	

TABLE II
GRATING PARAMETERS. (* = VALUE CHANGED IN THE CALCULATIONS)

Parameter	Symbol	A	B	C	D	Unit
Active region thickness (reg. 1)	$d_{a,1}$	80	80	*	60	nm
Active region thickness (reg. 2)	$d_{a,2}$	0	0	*	0	nm
Built-in effective index step	$\Delta n_{eff,ref}$	0.01	*	0.01	0.00831	
Confinement factor, active layer (reg. 1)	$\Gamma_{a,1}$	0.122	0.122	*	0.07	
Confinement factor, active layer (reg. 2)	$\Gamma_{a,2}$	0.0	0.0	*	0.0	
Material absorption, active region	α_a	2000	2000	2000	2000	m^{-1}
Material absorption, cladding layers	α_c	2000	2000	2000	2000	m^{-1}

given amount of coupling. The example serves to demonstrate that DFB lasers with index and gain coupling are not free of spatial holeburning and, as a consequence, the effective feedback of the optical field will depend on the bias conditions and the longitudinal position. It is therefore evident that a complex-coupled DFB laser cannot be characterized by a spatially independent coupling coefficient when operated above threshold.

A. Below Threshold

Fig. 4 gives a useful insight into the behavior of this type of complex-coupled DFB laser. It shows the locus curve for the complex coupling coefficient at threshold and also illustrates the change of the coupling coefficient as the carrier density is increased towards threshold (note the different scaling of the axes). Here the grating parameters in Column B of Table II were used. The horizontal line in the lower right part of Fig. 4 represents the case when there are no carriers injected into the active region (i.e., $g_m = -a N_0$). The left end of the line is for zero built-in index step ($\Delta n_{\mathrm{eff,\,ref}} = 0$), while a large index step is assumed at the right end ($\Delta n_{\mathrm{eff,\,ref}} = 0.022$). Going from left to right along the locus curve, each marked point corresponds to a change of the built-in index-step of 0.001.

As the bias current is increased the κ-value will change along the direction indicated by the arrows. The rate of change

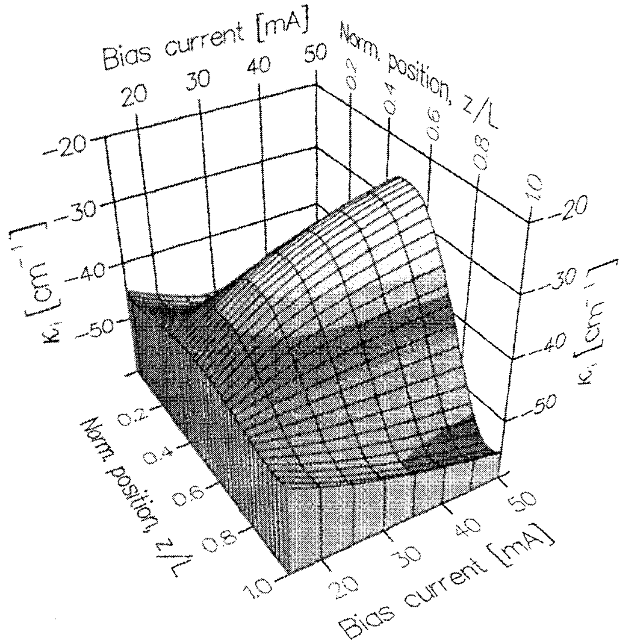

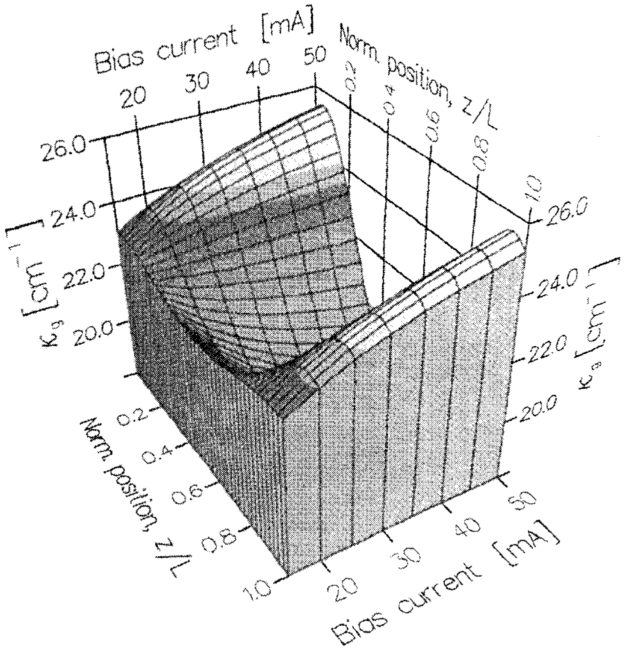

Fig. 3. Three-dimensional plots of (a) the index and (b) gain coupling coefficients as a function of the position and bias current in the region near threshold ($I_{th} = 13\,\text{mA}$).

is obtained from (9a) and (9b) as

$$\frac{d\kappa}{dN} = a\,\frac{\Delta\Gamma_a}{2\pi}\,(j - \alpha)\,\sin(\pi\gamma) \tag{15}$$

where α is the linewidth enhancement factor [34].

At some bias point the roundtrip gain will equal unity and the laser reaches threshold. The threshold condition is

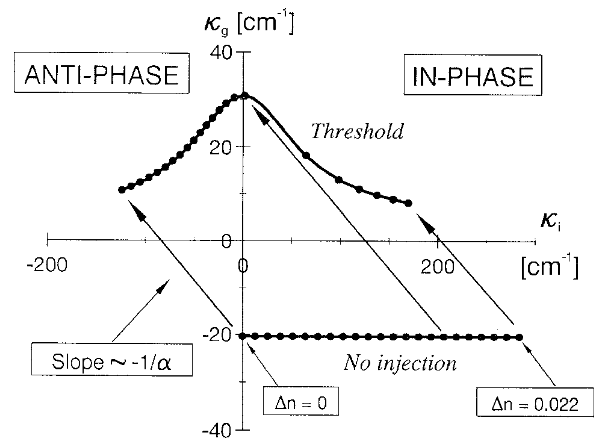

Fig. 4. Locus curves for the complex coupling coefficient when no carriers are injected (horizontal line) and at threshold (bell curve). The left and right ends of the locus curves correspond to built-in effective index steps of $\Delta n_{\text{eff, ref}} = 0.0$ and $\Delta n_{\text{eff, ref}} = 0.022$, respectively.

illustrated with the upper curve in Fig. 4. This curve is symmetrical with respect to the line $\kappa_i = 0$. It can be seen that a small built-in effective index step results in antiphase operation of the laser (opposite signs of the real and imaginary parts of κ), while a strong index grating results in in-phase operation at threshold. The actual shape of the threshold curve depends on the grating geometry, but the qualitative shape can easily be understood. For strong index coupling (positive or negative) a low threshold carrier density is expected, and this in turn results in a low threshold gain and a low gain coupling coefficient [cf. (9b)]. This is independent of the sign of the index coupling, so the curve has an even symmetry. On the other hand, when the index coupling is small, the feedback into the laser will have to be provided by the gain coupling. The gain coupling is proportional to the material gain, so that the threshold carrier density will have to be greater for small index coupling.

The maximum value of the gain coupling coefficient depends on the gain-grating thickness, duty-cycle, and the material gain, but with reasonable values of these parameters, κ_g cannot be made very large. Typically a maximum value of $\kappa_g L \simeq 1$ will be obtained. A critical range for the built-in index step is where the tangent of the threshold curve has a slope of $-1/\alpha$, cf. (15). Here a small change the in built-in index step will result in a large change in threshold gain, hence the strengths of the gain and index coupling. Furthermore, a small change in the carrier density caused by, for example, nonlinear gain, will cause a large change in coupling coefficients. We find that lasers designed in this region have a very poor slope efficiency close to threshold.

B. At Threshold

Fig. 5 shows the influence of the modulation depth of the active region on the index and gain coupling coefficients at threshold, for three values of the average active region thickness. The built-in effective index step is fixed at $\Delta n_{\text{eff, ref}} = 0.01$ (Column C of Table II). For deep modulation ($m > 0.5$), the gain coupling coefficient only varies slowly and

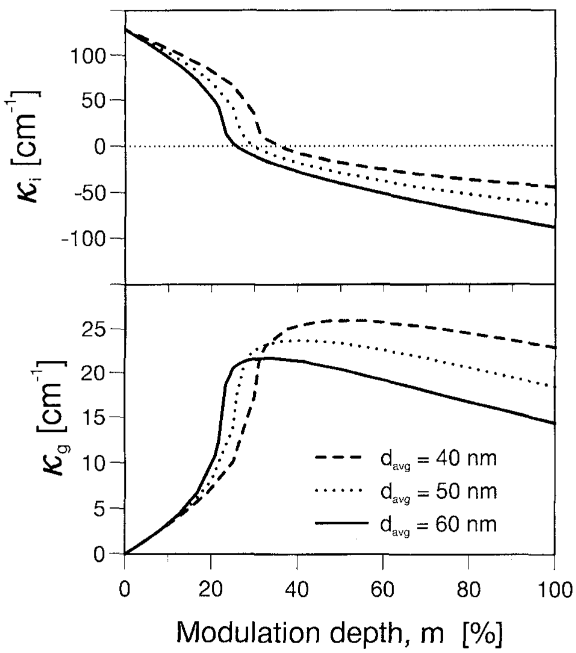

Fig. 5. Index and gain coupling coefficients at threshold versus active region modulation depth, m, for active region thicknesses, d_{avg}, of 40, 50, and 60 nm.

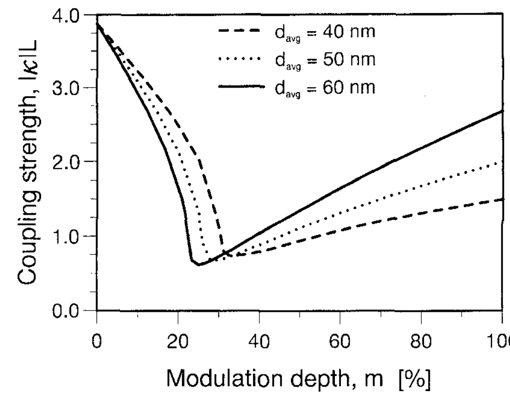

Fig. 6. Coupling strength, $|\kappa|L$, at threshold versus active region modulation depth, m, for active region thicknesses, d_{avg}, of 40, 50, and 60 nm.

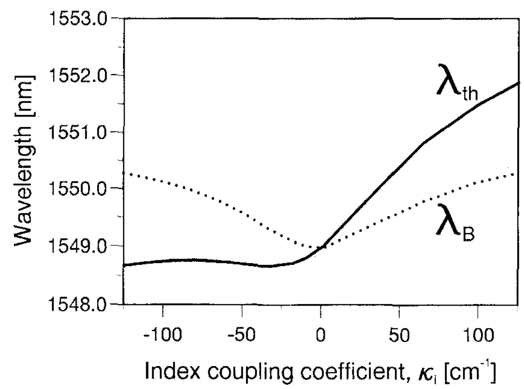

Fig. 7. Lasing wavelength, λ_{th}, and Bragg wavelength, λ_B, at threshold as a function of the index coupling coefficient, κ_i.

antiphase coupling is obtained. Fig. 6 shows the corresponding magnitude of the coupling strength. The coupling is at a minimum when the laser is purely gain-coupled. For on-off gratings ($m = 100\%$) we obtain $|\kappa|L = 2.7$ for a thick active region ($d_{\mathrm{avg}} = 60$ nm) and $|\kappa|L = 1.5$ for $d_{\mathrm{avg}} = 40$ nm.

Fig. 7 shows the variation of the lasing wavelength, λ_{th}, and the Bragg wavelength, λ_B, at threshold as a function of the index coupling coefficient, κ_i. The parameters are as for Fig. 4 (i.e., parameters according to Column B of Table II). As expected [1], the laser oscillates at the Bragg wavelength for pure gain coupling ($\kappa_i = 0$). The two extremes of the index coupling coefficient in Fig. 7 correspond to index steps of $\Delta n_{\mathrm{eff,ref}} = 0.0$ and $\Delta n_{\mathrm{eff,ref}} = 0.019$. For the antiphase case (i.e., $\kappa_i < 0$) the lasing wavelength is located on the short-wavelength side of the Bragg wavelength, while for in-phase operation the lasing wavelength is located on the long-wavelength side. Hence, the grating geometry and/or material parameters can tune the laser over a large portion of the stop-band [11].

V. Unstable Regions and Asymmetric Devices

Fig. 8 illustrates the above-threshold behavior of a typical complex-coupled antiphase laser. The laser structure parameters are in Table II and the grating structure are as in Column D of Table II which represents an on-off modulated active region. The threshold parameters are $I_{th} = 26$ mA and $\kappa = (-38 + j25)$ cm^{-1}. The output power from the left end-facet versus the bias current was obtained using the TWM. Close to threshold the laser oscillates in a stable and symmetrical mode. However, at a bias current of approximately 57 mA (10 mW of output power) two stable but asymmetric modes appear, and the symmetrical mode becomes unstable [19]. The two asymmetric modes have the same optical frequency, but the longitudinal distributions of the carrier and photon densities are mirror images of one another. Hence, the output powers from the two facets are reversed. This suggests that first the laser will turn on to a stable mode, but when operated at an output power higher than 10 mW this initial mode will become unstable and the laser will instead switch to an asymmetric mode. The asymmetric mode becomes nondominant for a bias current above 72 mA.

Fig. 9 shows output power waveforms from both facets and time-resolved frequency obtained using the TLLM. The bias current of the laser is taken through the following sequence: 30 mA for 15 ns, 70 mA for 15 ns, and finally 80 mA for 15 ns. When biased at 30 mA, the laser settles at a power of 1 mW with equal output from both facets after a very short turn-on transient. This is in the symmetrical regime, and the carrier density is longitudinally symmetrical. Going to 70 mA, the power initially increases to 14.2 mW corresponding to point A in Fig. 8. However, the output powers from the two facets soon start to diverge, and in steady state the output powers end up being 16.7 mW and 2.7 mW. This corresponds to a transition from point A to either B or C, according to the vertical arrows in Fig. 8. These powers are in good agreement with Fig. 8. The modal frequency, obtained using Fourier transforms with

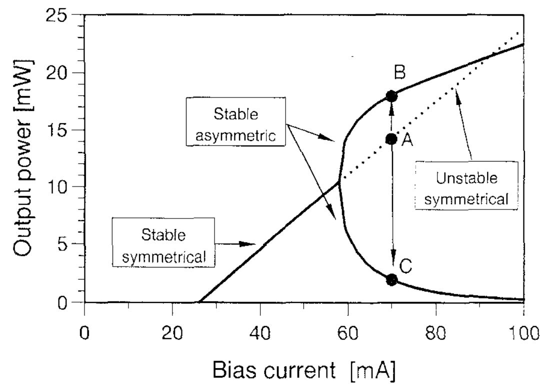

Fig. 8. Light-current characteristic of a symmetrical complex-coupled DFB laser with antiphase coupling. Stable and unstable modes are indicated in the Figure. The points "A," "B," and "C" refer to the time-domain simulation of Fig. 9.

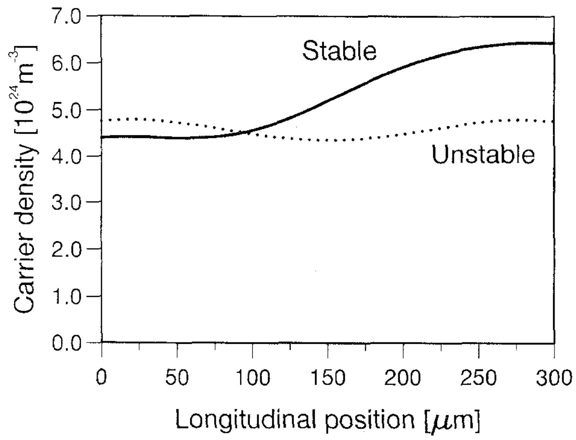

Fig. 10. Carrier density profile for unstable (dotted line) and stable (solid line) modes at 70 mA. The curves correspond to operation at points "A" and "B" in Fig. 8.

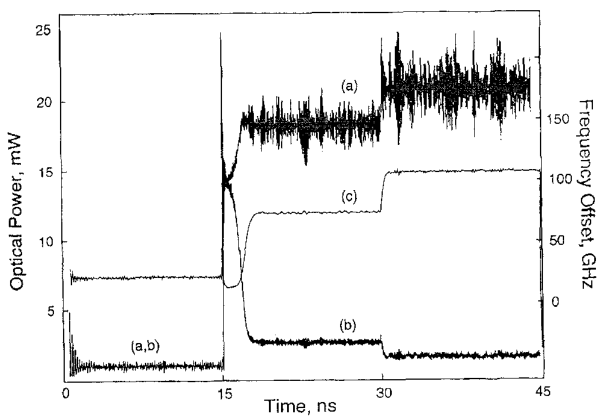

Fig. 9. Large-signal time domain simulation of the output power and instantaneous frequency for the laser in Fig. 8. Labels "(a)" and "(b)" indicate the output powers from the left and right facet and "(c)" is the instantaneous frequency.

a sliding time-window and then finding the peak frequency of the spectra, increases after an initial decrease. When the current is increased to 80 mA the asymmetry increases further and the modal frequency also increases. The corresponding carrier density profiles for the operating points A and B in Fig. 8 are illustrated in Fig. 10. A very large nonuniformity is observed for the asymmetric (stable) mode. The asymmetry in the power occurs in a random direction depending on the seed of the random noise generators which represent spontaneous emission in the TLLM. Thus, in practice, there would be a large uncertainty in the output power if such a laser were to be used in a digital transmission system. That is, the laser could turn on to point A and then move to either point B or C. This can be avoided by operating the laser below the critical power for instability.

Ideally, the critical power should be as high as possible when designing a laser. Using the TWM, we have mapped out regions where the laser is unstable when the modulation depth of the active region is varied. In Fig. 11 the grey-shaded area represents unstable operation and the lines indicate the critical power (i.e., the location of the pitchfork bifurcation in Fig. 8). The calculations were made with grating parameters as in Column C of Table II. It is seen by comparing Figs. 5 and 11 that these modal instabilities all occur for laser configurations with antiphase gain and index coupling. No instabilities were found for in-phase coupling. The critical power for instabilities can be increased by decreasing the modulation depth or average thickness of the active region, but instabilities cannot be eliminated if the laser geometry inherently leads to antiphase coupling. In Fig. 11 we have also indicated the critical powers for the cases where the modulation depth leads to a coupling ratio of -1.5 for a given thickness or duty cycle (dots). This ratio has been claimed to be the optimum value for high bandwidth and low chirp [4], [6], [15], [16]. It appears that when maintaining the coupling ratio, the critical power for instability cannot be changed dramatically by altering the average thickness of the active region, whereas reducing the duty cycle from 50% to 25% doubles the critical power. Reducing the duty cycle reduces the modulation bandwidth from 7.6 GHz to 6.3 GHz at 5 mW output power, possibly because the enhancement of differential gain, which gives the high bandwidth at this coupling ratio, relies on the dependence of index coupling on carrier density [4].

As mentioned above, the mode is nondominant for a bias current above 72 mA. This suggests that the dramatic increase in noise of the power traces in Fig. 9 is due to the laser being multimoded. A spectrum of the laser when operated at a dc bias current of 90 mA is shown in Fig. 12. This shows the growth of a side mode and a poor side mode suppression ratio. When the current was increased to 100 mA, the side mode suppression ratio reduced to almost zero dB, and the spectral peaks became broadened with many side bands spaced at around the laser relaxation oscillation frequency. In uniform DFB lasers, a strong side mode can reduce the excessive carrier density and thus is transitory, which leads to self-pulsations [35]. Self-pulsations were, however, not observed in this example.

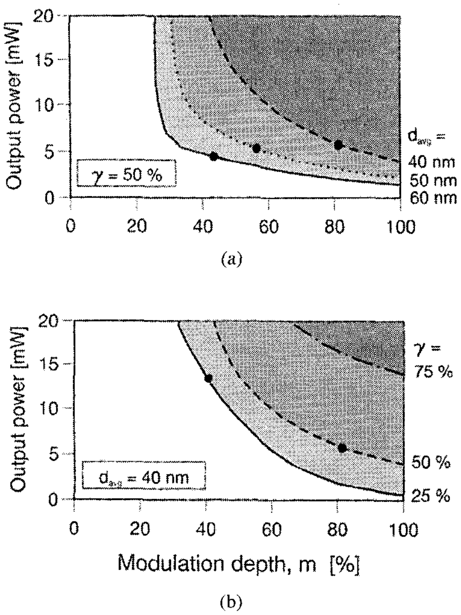

Fig. 11. Regions of unstable operation (grey area) for an antiphase complex-coupled DFB laser as a function of the active region modulation depth. (a) Grating duty cycle of $\gamma = 50\%$ for three thicknesses, and (b) average thickness $d_{\mathrm{avg}} = 40$ nm for three duty cycles. Points indicate critical powers for the particular geometries (thickness, duty cycle) which yield a coupling ratio, κ_i/κ_g, of -1.5 (at threshold).

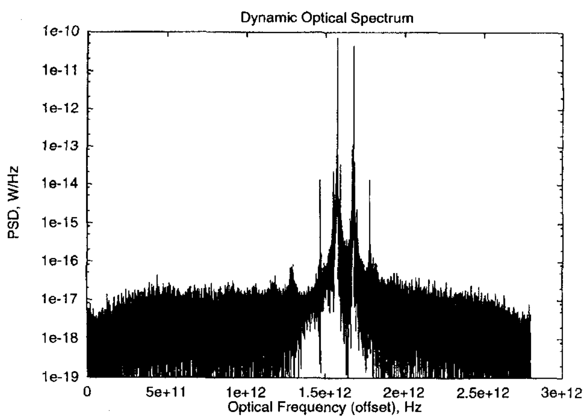

Fig. 12. Spectrum for the laser in Fig. 8 in the steady state, when operated at a dc bias of 90 mA.

By relaxing the symmetry requirement it might be possible to eliminate the instabilities. Indeed, it would be impossible to fabricate a perfectly symmetrical device. We analyzed a device with a left end-facet reflectivity at $R_1 = 1.0 \times 10^{-6}$ (as stated in Table I) and a variable right end-facet reflectivity, R_2. We found that even though the *perfect* longitudinal symmetry is broken, the laser still shows a behavior similar to that depicted in Fig. 8 [18]. The output power when the right end-facet reflectivity R_2 is increased to 1.0×10^{-3} (parameters according to Column D of Table II) is shown in Fig. 13. For a bias current above 50 mA the output power from the left end-facet will start to decrease (lower dashed curve), and the laser operation will resemble that in Fig. 8. The unstable mode

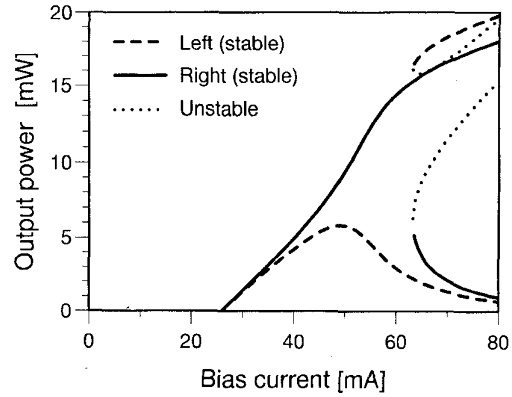

Fig. 13. Output power from the end facets as a function of the bias current when the reflectivities of the left and right end facets are $R_1 = 1.0 \times 10^{-6}$ and $R_2 = 1.0 \times 10^{-3}$, respectively.

now splits up into two parts (dotted curves) for the left and right end facets and a new stable mode will appear for bias currents above 63 mA. Furthermore, our calculations show that the stable modes of an asymmetric laser (with $R_1 < R_2$) will both become nondominant shortly after the appearance of the new modes. In the case shown in Fig. 13, a poor SMSR is obtained for operation above 70 mA.

VI. Physical Model

It is useful to try to obtain a simple physical understanding of the processes behind instabilities so that the laser can be modified to increase the critical power for instabilities.

The relaxation oscillation frequency and damping rate are fundamental quantities for semiconductor lasers. The damping rate at any point along the laser usually has two contributions, an almost constant term due to spontaneous recombination and a term which increases with the photon density. Schatz [17] studied the case of a perfectly symmetrical cavity, in which an asymmetric perturbation of the carrier density was deliberately introduced between the left and right halves of the cavity. Neglecting detailed spatial holeburning effects, the following rate equation for the time evolution of a small asymmetric perturbation ΔN was derived [(10) of [17] converted to our notation):

$$\frac{d}{dt}\Delta N = -\left(\frac{dR_{\mathrm{sp}}}{dN} + v_g S\left[\frac{1}{2}\frac{dg_m}{dN} + 2g\frac{dC_1}{dN}\right]\right)\Delta N. \quad (16)$$

Here, ΔN is the change of the carrier density relative to the symmetrical case, C_1 is a longitudinal fill factor giving the fraction of the total photon number contained in the left half of the cavity, $v_g = c/n_g$ is the group velocity, and dg_m/dN is the differential gain (in this case equal to the linear material gain coefficient a). The first two terms are the usual contributions to the damping rate as discussed above, which tend to damp out the perturbation. The third term represents the change of the fill factor with carrier density. This change is due to the carrier density dependence of the grating characteristics (transmittance and reflectance). We shall argue that for lasers oscillating on the short wavelength side of the Bragg wavelength the third term is negative (i.e., $dC_1/dN < 0$), which can make the damping rate negative above a critical output power. This means that perturbations will be amplified rather than attenuated, thereby favoring the transition to the asymmetric state.

To assess the carrier density dependence of the fill factor, we consider the example of Fig. 8 for a bias current of 70 mA and calculate the reflectances of the two ends of the laser seen from a reference plane in the center. Fig. 14 shows the magnitude of the reflectances r_L and r_R for the left and the right half of the cavity and the total roundtrip gain $|r_L r_R|$, when the laser is driven with a nonuniform (uniform) current to give an asymmetric (symmetrical) carrier density. The mode and side mode positions are shown as circles (nonuniform injection) and crosses (uniform injection) on the top curve, the mode being the one with a roundtrip gain of unity. The asymmetric and the symmetrical drive currents give almost the same lasing wavelengths. However, the left end has a significantly higher carrier density than the right end for the asymmetric drive current. This explains the increase in left reflectance and the shift of its maximum toward shorter wavelengths. The latter follows from the decrease in the Bragg wavelength with increasing carrier density. Conversely, the right reflectance is decreased and shifted toward longer wavelengths. As a result, we see a substantially larger difference in the left and right reflectances on the short wavelength side. The higher reflectance of the left hand section will reduce the penetration of the laser field into this section. The reduced stimulated emission allows the carrier density and hence the reflectance to increase further. This is a positive feedback situation which will drive the carrier density toward a stable point where the reflectance is high and the stimulated emission rate low, so that the gain of the positive feedback becomes zero in the steady state.

Equation (16) suggests that the critical power for instability can be increased if the spontaneous recombination rate is increased. To test this we altered the spontaneous carrier lifetime, $[dR_{\rm sp}/dN]^{-1}$, and calculated the critical power for instability. For this purpose only, the A- and C-coefficients were set to zero, and the B-coefficient was varied, cf. (13a). Hence, the spontaneous carrier lifetime is equal to $1/(2BN)$, where N is taken at threshold. For a spontaneous carrier lifetime of 0.52 ns we obtained a critical power of 6.3 mW, and for a lifetime of 0.21 ns we obtained 16.0 mW. The relaxation resonance frequency remained nearly unchanged at 7.6 and 7.7 GHz, respectively, for output powers of 5 mW. The product of the critical power and the carrier lifetime is almost constant. That is, there appears to be a critical energy for instability. Thus, the carrier lifetime could be decreased (by implantation with impurities, for example) to improve the laser's output power before instability. However, the cost is an increased threshold current.

VII. Conclusion

We have presented a generalized analysis of complex-coupled DFB lasers which gives the coupling coefficients in terms of the grating geometry and basic material parameters.

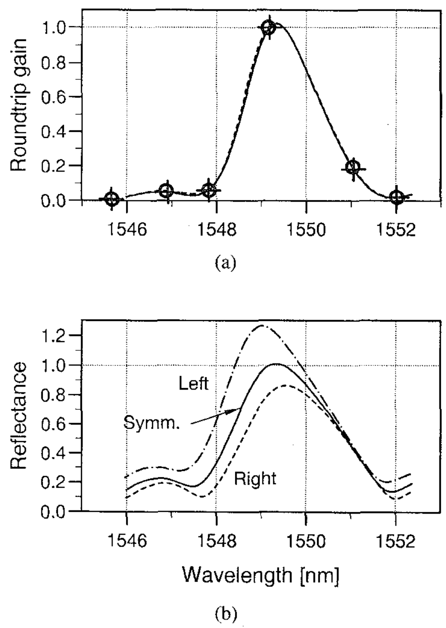

Fig. 14. Reflectance curves (filter functions) for the laser of Fig. 8 with uniform and slightly nonuniform injection. The total current is 70 mA in both cases, and in the asymmetric case the right current is 0.8 mA greater than the left current. (a) Roundtrip gain ($|r_L r_R|$) and mode positions. Solid curve and crosses: uniform injection, dashed curve and circles: nonuniform injection. (b) Reflectance curves ($|r_L|$ and $|r_R|$) of the left and right halves of the cavity seen from the reference plane. For uniform injection the cavity is symmetric and the curves coincide.

We have shown that two independently derived models give excellent agreement for complex-coupled DFB lasers.

Our analysis shows that lasing on the short-wavelength side of the Bragg wavelength can lead to instabilities in complex-coupled DFB lasers. The fact that some lasers may turn on in a (nearly) symmetrical mode and subsequently switch to a mode of high/low or low/high power from the two facets can lead to undesirable behavior in an optical communication system, because the power and the wavelength are not well defined. Similar instabilities in index-coupled DFB lasers have been shown previously. In particular, we conclude that a complex-coupled laser optimized for maximum modulation bandwidth (i.e., with a coupling ratio of $\kappa_i/\kappa_g \simeq -1.5$) may become unstable at an output power of less than 10 mW. In addition, for nonsymmetrical cavities, operation on the short wavelength side of the Bragg wavelength may lead to highly distorted light-current characteristics and poor SMSR at moderate output power.

We have shown that the duty cycle of the active region grating can be reduced to increase the critical power for instability, but with a reduction in modulation bandwidth. However, it appears that all antiphase lasers are bound to become unstable at a finite power. A simple explanation for the instabilities highlights the importance of spontaneous recombination in preventing instabilities at low powers, but other damping mechanisms might also have a positive influence. The critical power for instability is inversely proportional to the carrier lifetime, which is in broad agreement with a previous analysis of index-coupled DFB lasers [17]. Interestingly, the modulation bandwidth for a given power is not reduced by this method of increasing the critical power for instability.

In conclusion, although the critical power for instability can be increased while keeping a high modulation bandwidth by appropriate design, antiphase lasers with an optimized coupling ratio for high bandwidth and low chirp will always become unstable at some power. However, in-phase complex-coupled DFB lasers are stable, but they do not have the same bandwidth enhancement mechanism.

REFERENCES

[1] H. Kogelnik and C. V. Shank, "Coupled-wave theory of distributed feedback lasers," *J. Appl. Phys.*, vol. 43, pp. 2327–2335, May 1972.
[2] K. David, G. Morthier, P. Vankwikelberge, R. G. Baets, T. Wolf, and B. Borchert, "Gain-coupled DFB lasers versus index-coupled and phase-shifted DFB lasers: A comparison based on spatial hole burning corrected yield," *IEEE J. Quantum Electron.*, vol. 27, pp. 1714–1723, June 1991.
[3] W. T. Tsang, F. S. Choa, M. C. Wu, Y. K. Chen, R. A. Logan, N. G. Chu, A. M. Sergent, and C. A. Burrus, "Semiconductor distributed feedback lasers with quantum well or superlattice gratings for index or gain-coupled optical feedback," *Appl. Phys. Lett.*, vol. 60, pp. 2580–2582, May 1992.
[4] K. Kudo, J. I. Shim, K. Komori, and S. Arai, "Reduction of effective linewidth enhancement factor $\alpha_{\rm eff}$ of DFB lasers with complex coupling coefficients," *IEEE Photon. Technol. Lett.*, vol. 4, pp. 531–534, June 1992.
[5] X. Pan, B. Tromborg, H. Olesen, and H. E. Lassen, "Effective linewidth enhancement factor and spontaneous emission rate of DFB lasers with gain coupling," *IEEE Photon. Technol. Lett.*, vol. 4, pp. 1213–1215, Nov. 1992.
[6] A. J. Lowery, "Large-signal effective α factor of complex-coupled DFB semiconductor lasers," *Electron. Lett.*, vol. 28, pp. 2295–2296, Dec. 1992.
[7] L. M. Zhang, J. E. Carroll, and C. Tsang, "Dynamic response of the gain-coupled DFB laser," *IEEE J. Quantum Electron.*, vol. 29, pp. 1722–1727, June 1993.
[8] K. Kudo, S. Arai, and J. I. Shim, "Linewidth reduction of DSM lasers due to effects of composite cavity and distributed reflectors," *IEEE J. Quantum Electron.*, vol. 29, pp. 1769–1781, June 1993.
[9] G. P. Li and T. Makino, "Single-mode yield analysis of partly gain-coupled multiquantum-well DFB lasers," *IEEE Photon. Technol. Lett.*, vol. 5, pp. 1282–1284, Nov. 1993.
[10] K. Kudo, S. Arai, and K. C. Shin, "The optical gain coupling saturation effect on the linewidth property of complex coupled DFB lasers," *IEEE Photon. Technol. Lett.*, vol. 6, pp. 482–485, Apr. 1994.
[11] A. J. Lowery and D. Novak, "Performance comparison of gain-coupled and index-coupled DFB semiconductor lasers," *IEEE J. Quantum Electron.*, vol. 30, pp. 2051–2063, Sept. 1994.
[12] T. K. Sudoh, M. Funabashi, Y. Nakano, K. Tada, and T. Hirata, "Dynamics of gain-switching operation in gain-coupled distributed-feedback semiconductor lasers with absorptive grating," *IEEE J. Selected Topics Quantum Electron.*, vol. 1, pp. 583–591, June 1995.
[13] A. Rast, T. W. Johannes, W. Harth, and G. Franz, "A new complex-coupled DFB-laser with a contacted surface grating for $\lambda = 1.55$ μm," in *Proc. IEEE Optoelectronics.*, vol. 142, no. 3, 1995, pp. 162–164.
[14] J. Zoz, T. W. Johannes, A. Rast, B. Borchert, U. Barabas, and W. Harth, "Dynamics and stability of complex-coupled DFB lasers with absorptive gratings," *IEEE J. Quantum Electron.*, vol. 31, pp. 1432–1442, Aug. 1995.
[15] A. J. Lowery and D. Novak, "Enhanced maximum intrinsic modulation bandwidth of complex-coupled DFB semiconductor lasers," *Electron. Lett.*, vol. 29, pp. 461–463, Mar. 1993.
[16] L. M. Zhang and J. E. Carroll, "Enhanced AM and FM modulation response of complex coupled DFB lasers," *IEEE Photon. Technol. Lett.*, vol. 5, pp. 506–508, May 1993.
[17] R. Schatz, "Longitudinal spatial instability in symmetric semiconductor lasers due to spatial hole burning," *IEEE J. Quantum Electron.*, vol. 28, pp. 1443–1449, June 1992.
[18] H. Olesen, B. Tromborg, H. E. Lassen, and X. Pan, "Mode instability and linewidth rebroadening in DFB lasers," *Electron. Lett.*, vol. 28, pp. 444–446, Feb. 1992.
[19] H. Olesen, B. Tromborg, X. Pan, and H. E. Lassen, "Stability and dynamic properties of multi-electrode lasers using a Green's function approach," *IEEE J. Quantum Electron.*, vol. 29, pp. 2282–2301, Aug. 1993.
[20] A. J. Lowery and H. Olesen, "Dynamics of mode-instabilities in quarter-wave-shifted DFB semiconductor lasers," *Electron. Lett.*, vol. 30, pp. 965–967, June 1994.
[21] A. J. Lowery, B. Jonsson, H. Olesen, and D. Novak, "Mode instabilities in complex-coupled DFB semiconductor lasers," *Electron. Lett.*, vol. 31, pp. 40–41, Jan. 1995.
[22] B. Tromborg, H. E. Lassen, and H. Olesen, "Traveling wave analysis of semiconductor lasers: Modulation responses, mode stability and quantum mechanical treatment of noise spectra," *IEEE J. Quantum Electron.*, vol. 30, pp. 939–956, Apr. 1994.
[23] A. J. Lowery, A. Keating, and C. N. Murtonen, "Modeling the static and dynamic behavior of quarter-wave-shifted DFB lasers," *IEEE J. Quantum Electron.*, vol. 28, pp. 1874–1883, Sept. 1992.
[24] A. J. Lowery and D. F. Hewitt, "Large-signal dynamic model for gain-coupled DFB lasers based on the transmission-line model," *Electron. Lett.*, vol. 28, pp. 1959–1960, Oct. 1992.
[25] G. P. Li, T. Makino, R. Moore, N. Puetz, K.-W. Leong, and H. Lu, "Partly gain-coupled 1.55 μm strained-layer multiquantum-well DFB lasers," *IEEE J. Quantum Electron.*, vol. 29, pp. 1736–1742, June 1993.
[26] T. R. Chen, P. C. Chen, J. Ungar, and N. Bar-Chaim, "High speed complex-coupled DFB laser at 1.3 μm," *Electron. Lett.*, vol. 30, pp. 1055–1057, 1994.
[27] B. Borchert, B. Stegmüller, and R. Gessner, "Fabrication and characterization of improved strained quantum-well GaInAlAs gain-coupled DFB lasers," *Electron. Lett.*, vol. 29, pp. 210–211, Jan. 1993.
[28] R. Baets, K. David, and G. Morthier, "On the distinctive features of gain coupled DFB lasers and lasers with second-order grating," *IEEE J. Quantum Electron.*, vol. 29, pp. 1792–1798, June 1993.
[29] X. Pan, B. Tromborg, and H. Olesen, "Complex pole expansion approach to multimode DFB laser modeling," *IEE Proc. J. Optoelectronics,* vol. 141, pp. 271–274, Aug. 1994.
[30] H. Lage, J. Salzman, H. Olesen, B. Jonsson, J. Hanberg, A. Møller-Larsen, and O. Albrektsen, "Direct measurement of the local intensity modulation response of distributed feedback lasers," *IEEE Photon. Technol. Lett.*, vol. 7, pp. 260–262, Mar. 1995.
[31] B. Christensen, H. Olesen, B. Jonsson, H. Lage, J. Hanberg, O. Albrektsen, and A. Møller-Larsen, "Detailed mapping of the local IM and FM responses of DFB lasers," *Electron. Lett.*, vol. 31, pp. 799–800, May 1995.
[32] J. Salzman, H. Olesen, A. Møller-Larsen, O. Albrektsen, J. Hanberg, J. Nørregaard, B. Jonsson, and B. Tromborg, "Distributed feedback lasers with an S-bent waveguide for high-power single-mode operation," *IEEE J. Selected Topics Quantum Electron.*, vol. 1, pp. 346–355, June 1995.
[33] A. J. Lowery, "Transmission-line modeling of semiconductor lasers: The transmission-line laser model," *Int. J. Numer. Model,* vol. 2, pp. 249–265, Dec. 1989.
[34] C. H. Henry, "Theory of the linewidth of semiconductor lasers," *IEEE J. Quantum Electron.*, vol. QE-18, pp. 259–264, Feb. 1982.
[35] A. J. Lowery, "Dynamics of SHB-induced mode-instabilities in uniform DFB semiconductor lasers," *Electron. Lett.*, vol. 29, pp. 1852–1853, Oct. 1993.

Björn Jonsson was born in Stockholm, Sweden, on August 28, 1960. He received the M.Sc. degree in engineering physics and the Ph.D. degree in optoelectronics from Chalmers University of Technology, Göteborg, Sweden, in 1986 and 1992, respectively. His thesis work focused on strong optical nonlinearities in quantum well material.

In 1993, he was employed as a Postdoctoral Research Associate at the Department of Optical Communications, Tele Danmark Research, where his field of research has been numerical modeling of optoelectronic components, focusing on multielectrode DFB lasers for high-speed communication systems. This work continued until the end of 1995, when research on analysis and fabrication of optoelectronic components was terminated at Tele Danmark. He is now in the "Access networks" section of Tele Danmark R&D.

Arthur James Lowery (SM'95) was born in Yorkshire, England, on October 17, 1961. He was awarded a First Class Honors degree in applied physics from Durham University, England, in 1983. He received the Ph.D. degree ("Transmission-Line Modeling of Semiconductor Lasers") in 1988 from the University of Nottingham, England.

He then worked as a Systems Engineer at Marconi Radar Systems, where he become interested in optical fiber communication systems. In 1984, he was appointed as a University Lecturer at the University of Nottingham, England. In 1990, he moved to Australia to take up a position as a Senior University Lecturer in the newly formed Photonics Research Laboratory at the University of Melbourne, which is now part of Australian Cooperative Research Center. In January 1993, he was promoted to Associate Professor and Reader at the University of Melbourne. He has published more than 100 research papers in the fields of photonics and numerical modeling, and has one patent on the design of mode-locked lasers.

Dr. Lowery was awarded the ATERB Medal for being the Outstanding Young Investigator of the year by the Australian Telecommunications and Electronics Research Board in 1995. His research interests include photonic CAD, mode-locked lasers, laser amplifiers, photonic switching and transmultiplexing, fiber video distribution, industrial ranging systems, and semiconductor laser design. He is a Chartered Engineer, and a Member of the Institute of Electrical Engineers.

Henning Olesen was born in Vinderup, Denmark, on October 11, 1955. He received the M.Sc. degree in electrical engineering in 1980 and the Ph.D. degree in 1982, both from the Technical University of Denmark, Lyngby, Denmark.

From 1982 to 1984, he was a Postdoctoral Research Associate at the Electromagnetics Institute, Technical University of Denmark, where he worked on coherent optical transmission systems, in particular the coherence and FM characteristics of semiconductor lasers. In 1983, he was a Visiting Scientist at Musashino ECL, Nippon Telegraph and Telephone Corporation, Tokyo, Japan. In 1984, he joined Tele Danmark Research (at that time named TFL Telecommunications Research Laboratory), Hørsholm, Denmark, and from 1991 until the end of 1995 he was the Project Manager for modeling and characterization of optoelectronic components. In 1992, he was on leave at the Opto-electronics Research Laboratories, NEC Corporation, Tsukuba, Japan. His research has primarily been concerned with development of theoretical models for advanced semiconductor lasers and with design and simulation of high-speed singlemode DFB lasers. He has written or coauthored more than 75 scientific journal and conference publications. At the end of 1995, research on analysis and fabrication of optoelectronic components was terminated at Tele Danmark; he is now in the "Multimedia" section of Tele Danmark R&D.

Dr. Olesen has served as the Guest Editor for a special issue of *IEEE Proceedings, Journal of Optoelectronics* (April 1994), entitled "Semiconductor Optoelectronics" and as the Danish MC member for the European COST 240 program on photonic components.

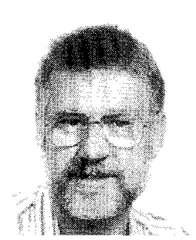

Bjarne Tromborg (A'88–M'89) was born in 1940 in Denmark. He received the M.Sc. degree in physics and mathematics from the Niels Bohr Institute, Copenhagen, Denmark in 1968.

From 1968 to 1977, he was a Research Associate at NORDITA and the Niels Bohr Institute. His research field was theoretical elementary particle physics, in particular analytic S-matrix theory and electromagnetic corrections to hadron scattering. He co-authored a research monograph on dispersion theory. From 1977 to 1979, he taught at a high school. In 1979, he joined Tele Danmark Research (at that time named TFL) in Hørsholm, and he was Head of the Optical Communications Department from 1987 until the end of 1995. He has been associated with the University of Copenhagen as an Adjunct Professor in physics since 1991. His research interests include physics and technology of optoelectronic devices. At the end of 1995, research on analysis and fabrication of optoelectronic components was terminated at Tele Danmark; he is now in the "Transmission" section of Tele Danmark R&D.

Mr. Tromborg is presently TPC member at the conferences IPR '96, CLEO/Europe '96, and ISLC '96. He is Short Course Chair at CLEO/Europe '96, member of the board of the Materials Center for Microelectronics, Technical University of Denmark, member of the board of the Photonics Center, Royal Institute of Technology, Sweden, and member of the Danish Natural Science Research Council. He received the Electroprize from the Danish Society of Engineers in 1981 and was recently awarded the Lady Davis Visiting Professorship for nine months at Technion, Haifa, Israel, in 1996–1997.